Ice lithography using tungsten hexacarbonyl

Haque, Rubaiyet I.; Waafi, Affan Kaysa; Chang, Bingdong; Han, Anpan

Published in:
Micro and Nano Engineering

Link to article, DOI:
10.1016/j.mne.2023.100171

Publication date:
2023

Document Version
Publisher's PDF, also known as Version of record

MNE 18 (2023) 100171

Contents lists available at ScienceDirect

Micro and Nano Engineering

journal homepage: www.sciencedirect.com/journal/micro-and-nano-engineering

Ice lithography using tungsten hexacarbonyl

Rubaiyet I. Haque, Affan Kaysa Waafi, Bingdong Chang, Anpan Han *

Department of Mechanical Engineering, Technical University of Denmark, 2800 Kongens Lyngby, Denmark.

ARTICLE INFO

Keywords:
Ice lithography
Tungsten hexacarbonyl
Electron beam lithography
Nanofabrication
Organic ice

ABSTRACT

Ice lithography (IL) fabricates 2D and 3D patterns using electron-solid interaction principle. Herein, we report IL patterning of the negative tone metalorganic precursor. The precursor is condensed at 80 K. It is then patterned using a 5–20 keV electron beam. The pattern thickness and surface roughness increase with area dose. The line thickness and linewidth also increase with the growing line doses. XPS results show that tungsten is bound to oxygen; metallic and WC bonds are absent, which suggests the IL patterned tungsten hexacarbonyl contains oxidized tungsten embedded in carbon and oxygen matrix. Finally, the IL patterned tungsten hexacarbonyl was investigated as an etch mask for nanofabrication applications. The silicon plasma etching selectivity is 30:1, comparable with commercial photoresists.

1. Introduction

Ice lithography (IL), which uses electron-solid interaction principles, is an emerging direct-write technique for nano- and micro-scale fabrication at high resolution on various substrates [1–4]. In 2022, Wu and colleagues demonstrated layer-by-layer 3D printing [4]. The IL process (Fig. 1a) composes the creation of organic ice resist layer by condensing organic precursor gas at cryogenic temperatures on the substrate under vacuum, followed by cross-linking using high energy focused electron beam (e-beam) exposure. Three fundamental constituents associated with ice lithography are: energetic electrons, condensing gasses inside the vacuum, and electron matter interactions [5,6]. Organic ice, such as octane [7], and nonane ice [6–8], is usually a negative resist [9], while water ice [10] acts as a positive resist. During the condensation process, the ice thin-film forms on the substrate maintained at cryogenic temperature. The external source of high-energy electrons facilitates electrochemical reactions. The energetic electrons cause bond scissions, creating small and large radicals. The larger radicals can recombine or react with other molecules to form large molecular networks, whereas the smaller radicals may vaporize or recombine with large networks [7]. Finally, evaporation removes excess materials without any residue. IL advantages are discussed in detail in the references, and we highlight three advantages; (i) IL enables the processing of very fragile samples such as suspended carbon nanotubes [2], (ii) layer-by-layer processing for 2.5 D lithography [4,8], (iii) IL is 4 orders of magnitude faster than focused electron beam induced deposition (FEBID) [8]. Faster process is confirmed by De Teresa and colleagues, that showed speed of organometallic ices cross-linking using ion-beams (cryo-FIBID) increases by several orders of magnitude compared with gas-based processes [11,12]. Since the IL process uses electron and solid interaction, it is 1000 times faster than the FEBID, which is based on electron-gas-substrate interactions [9]. Bresin et al. used Pt precursors at cryogenic temperatures [13].

Herein, we report IL using organometallic tungsten hexacarbonyl precursor (Fig. 1b), which is an inexpensive and well-characterized metalorganic precursor. We selected the tungsten hexacarbonyl precursor because it has been studied by both FEBID [14–16] and Cryo-FIBID [11], and we could compare different methods. Dose optimization was performed for area- and line-patterning, followed by X-ray photoelectron spectroscopy (XPS) characterization of chemical components and the demonstration of IL tungsten as a mask for silicon etching.

2. Materials and methods

IL is performed using a custom-made ice lithography system based on a Hitachi FlexSEM 1000 with a customized cryostage and gas injection system (GIS) [17]. Tungsten hexacarbonyl ($W(CO)_6$, 99%) is purchased from Acros Organic, Thermo Fisher Scientific. At ambient conditions, tungsten carbonyl forms solid crystals. Following the Antonie equation, the vapor pressure of tungsten carbonyl follows the relation $log_{10}P = 12.094 - 4077/T$ for the temperature range of 301 to 308 K, whereas for the temperature range between 353 and 423 K, follows the relation $log_{10}P = 11.523 - 3872/T$. Here, T and P refer to temperature in K and pressure in Torr [18]. A stainless-steel vial is filled with 5 mg of $W(CO)_6$

* Corresponding author.
E-mail address: anph@mek.dtu.dk (A. Han).

https://doi.org/10.1016/j.mne.2023.100171
Received 29 September 2022; Received in revised form 19 December 2022; Accepted 13 January 2023
Available online 14 January 2023

precursor, and the vial is attached to the GIS. The vial is equipped with a 12.5 W heating pad (RS pro Silicon Heater Mat) that heats up to 573 K. Vacuum pump is employed to remove air from the GIS system. We raised the precursor housing temperature to ~333 K. As a result, the tungsten precursor sublimes inside the GIS due to high temperature and low pressure. The vapor pressure of the precursor in the GIS is monitored and measured using the pressure gauge (piezo vacuum gauge, 902B-42,014 from MKS Instruments) until desired vapor pressure is achieved. On-demand, the injection valves are actuated to allow precise control of the precursor gas flow into the SEM vacuum chamber through the nozzle attached just above the substrate. A custom-made LabVIEW program controls the automated gas injection system.

Silicon (Si) substrates coated with a silicon dioxide (SiO_2) layer are used as a substrate during the IL process. The vacuum chamber of the SEM is maintained at 1×10^{-5} mbar. While in operation, the cryostage, connected to the liquid nitrogen (LN_2) tank, cooled down to below 80 K along with the substrate. The cold finger, used to shield the sample from vacuum contaminants, is mechanically attached to the cryostage and thus maintained at around a temperature as cryostage. Since the silicon substrate is placed on the cryogenic stage. The rapid condensation of W$(CO)_6$ gas takes place at temperatures well below the glass transition temperature (T_g), and thus produces a thin-film of amorphous ice during the condensation process [19].

To evaluate the dose-response behavior of W$(CO)_6$, the ice lithography system is connected to ELPHY Quantum and ELPHY Plus PC system from Raith GmbH. The electron beam current was measured using a Faraday cup connected to a picoammeter and held constant at 800 pA while patterning. Dose tests are performed with proximity correction. Because our SEM does not have a beam blanker, delays in the pattern generator system can be visible when writing at 5 keV and low dose.

Patterned micro- and nanostructures were studied using a scanning electron microscope (SEM, Zeiss Supra VP 40) equipped with energy dispersive X-ray spectroscopy (EDS) spectroscopy from Oxford. XPS Nexsa system (Thermo Fisher Scientific Inc.) is used, and it is equipped with a monochromatic Al K-alpha photon source at 1486.6 eV, and the spot size was set to be around 200 μm. Atomic force microscope (AFM) was a Dimension Icon-PT from Bruker AXS. The etching performance was investigated with an inductively coupled plasma (ICP) etching system SPTS MP0637 (SPTS Technologies, Ltd.). Parameter settings for the Bosch process are etch step having a duration of 3 s with SF_6 gas flow of 40 sccm and platen power of 40 W, followed by the deposition step having a duration of 3.2 s with C_4F_8 gas flow of 50 sccm, coil power is set to be 1 kW during the whole process.

3. Results and discussions

Tungsten hexacarbonyl is condensed to a solid at 80 K (Fig. 2). Fig. 2a shows the dedicated silicon substrate patterned with Au electrodes and cut by a diamond blade. This substrate creates good contrast in the SEM. The material contrast is generated by the conductive Au electrodes and the bright silicon dioxide charged by the imaging electron beam. The diamond blade cut provides the geometrical contrast. Fig. 2b shows the 100-nm-thick tungsten hexacarbonyl ice condensed onto the substrate. The material contrast becomes nearly invisible, and we still clearly see the geometrical contrast. Fig. 2b shows the tungsten precursor ice is amorphous. The amorphous state of such layer at low temperatures is stabilized by the high viscosity and the small value of the stationary nucleation rate of the crystal phase. The ice started to sublime at 253 K.

The GIS is calibrated for the W$(CO)_6$ precursor to relate the pressure drop in GIS and resist ice layer thickness formation on the substrate, as described in [6]. Fig. 3 presents the calibration curve of the GIS for the W$(CO)_6$ precursor. Matching our previous work with other organic ices [6], the cross-linked W$(CO)_6$ thickness is directly proportional to the GIS pressure drop.

Following the deposition, the tungsten precursor ice layer is patterned using energized electronics source from SEM. The W—C bond-

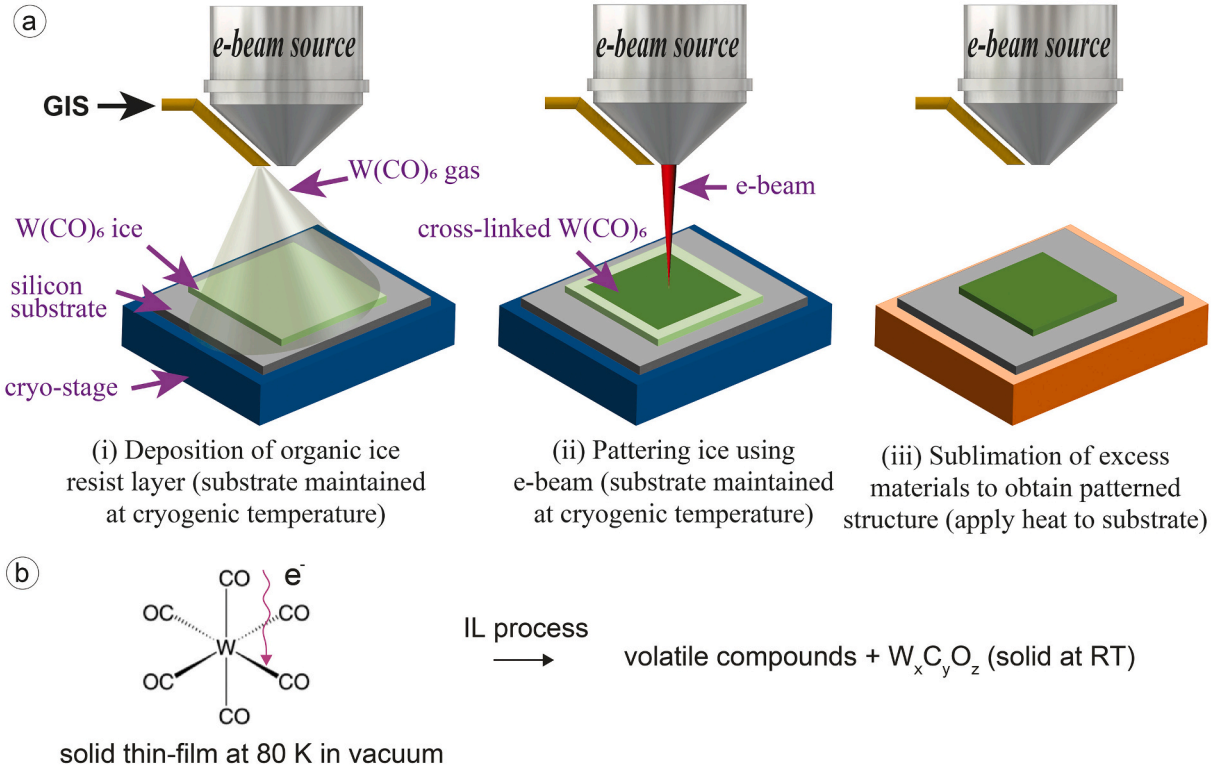

Fig. 1. (a) Schematics of the ice lithography process using tungsten hexacarbonyl. (b) IL processing of W$(CO)_6$ ice into tungsten-containing solids at room temperature.

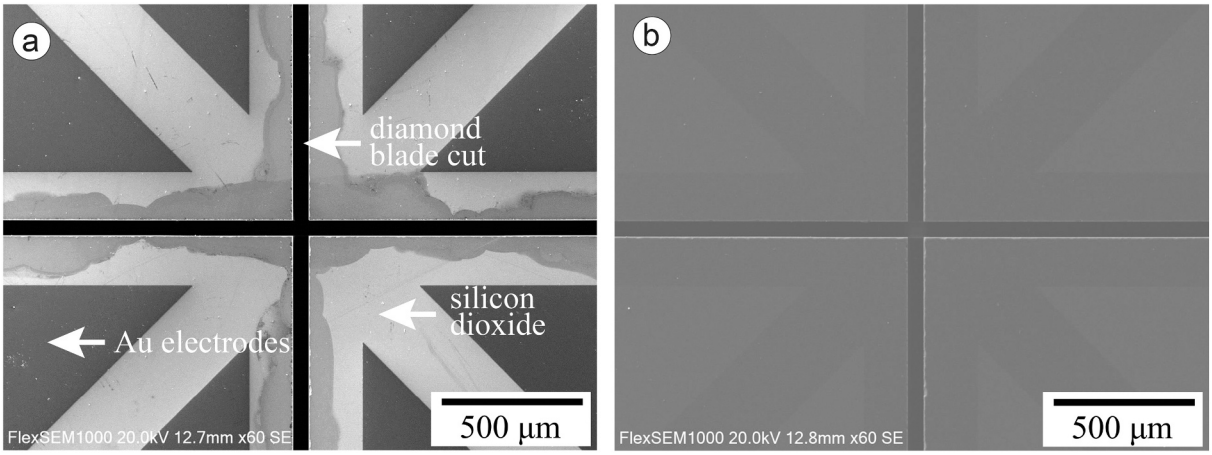

Fig. 2. (a) SEM image of silicon substrate with metal electrodes. (b) 100-nm-thick tungsten hexacarbonyl ice was condensed onto the substrate at 80 K and imaged at 20 keV.

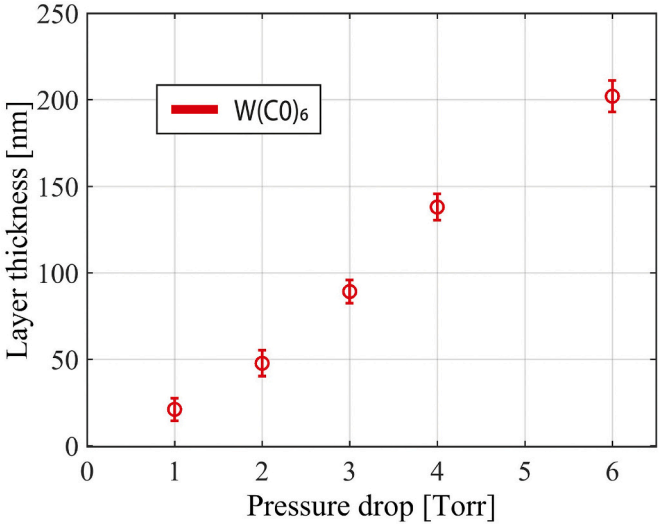

Fig. 3. Calibration curve for $W(CO)_6$ OIR thickness. The thickness of exposed OIR measured by AFM is proportional to the pressure drop in the GIS cell.

dissociation energy (BDE) of tungsten carbonyls is 5.289 eV [20]. The energized electron interacts with the solid resulting in the energy exchange between them and leading to the electrochemical reactions. Several parameters, namely, density, molecular weight, and thickness of the organic ice layer, along with the electron beam energy, beam diameter, beam current, and pixel dwell-time, are associated with ice lithography. The two most important parameters of the electron beam source are acceleration voltage and beam current. The acceleration voltage controls the primary electron (PE) energy of the e-beam, and the beam current controls the number of electrons per unit of time. The beam current is proportional to the square of the beam diameter (D_b). Another important factor is the thickness of the resist layer. The thicker resist layer provides greater interaction volume between the resist and the electrons. Therefore, the exposure dose also depends on the thickness of the resist film. To limit the number of variables, we keep the beam current and resist thickness constant.

For the dose test, 100-nm-thick tungsten carbonyl ice is frozen onto the silicon substrate. An array of twenty squares having area of 5 × 5 μm^2 with an inter-square spacing of 5 µm were patterned at different area doses from 0.1 to 1000 mC/cm^2 (Fig. 4). The electron energy is 5, 10 and 20 keV. The area dose is defined as $D_A = I_{0A}\tau_A/A$, being the number of electrons that are applied to a unit area. Area dose is related to patterning speed, where I_{0A} is the beam current, τ_A is the dwell time per dot, and A refers to the exposed area. Following the sublimation process, the patterned layers' thickness was characterized, and the critical area doses were determined. AFM analysis was performed to create the contrast curve to measure the critical dose accurately.

Fig. 4a presents the AFM images of the cross-linked tungsten precursor patterns, and they indicate the exposure quality and estimate the critical dose. The patterns are very smooth at low area doses, and at higher area doses, the patterns become rough. At the highest dose, we observed partial delamination of the cross-linked patterns from the substrate, which gives a higher surface roughness, this is most likely caused by carbon monoxide dissociation and evaporation of other volatile compounds. This phenomenon is different compared with other negative tone resists, like HSQ [21] and epoxy resist [22], AFM data analysis confirms that the thickness and surface roughness of the cross-linked square pattern increases with the increasing area dose. The area dose curve (Fig. 4b) shows that at 5 keV, 20 mC/cm^2 is needed to fully cross-link a 100-nm-thick $W(CO)_6$ ice layer. The dose is higher for 10 and 20 keV, which agrees well with our previous studies [8]. The dose needed to cross-link $W(CO)_6$ is 3 times higher than for organic ices without metals. The cross-linking throughput is still 3 orders of magnitudes larger than FEBID [8].

Additionally, the trend shows that the surface roughness of the cross-link pattern area also increases with the increasing area dose (Fig. 4c). At the critical dose, the RMS surface roughness is between 5 and 10 nm, which is higher than e.g., nonane (1 nm RMS). Lower PE energies yield the smoothest cross-linked films. Hence, for applications requiring smooth surface finishing, the exposure dose should be slightly below the critical dose, and low primary electron energy is preferred. The critical dose to cross-link $W(CO)_6$ is 50 $\mu C/cm^2$ for cryo-FIBID using Ga^+ [11] and this is because ions are much more efficient in generating secondary electrons needed for chemical cross-linking.

To further study the IL processing of tungsten hexacarbonyl, arrays of lines with the length of 5 µm and an inter-square spacing of 5 µm were patterned at different doses from 1 nC/cm to 100 µC/cm (Fig. 5). The primary electron energies were 5, 10, and 20 keV. The line-dose is defined as $D_L = I_{0L}\tau_L/\Delta x_L$, where I_{0L} is the beam current, τ_L is the dwell time per dot, and $\Delta x_L = L/N$. Here, L and N refer to the length and the number of dots in the line, respectively.

Fig. 5a presents the AFM images of the cross-linked tungsten precursor line patterns. Similar to area-dose, the lines are very smooth at low line-dose, and the patterns become very rough at high line-dose. Adhesion of cross-linked tungsten precursor was excellent. The patterns are severely damaged for the highest dose, and we observed significant material losses. Because we used a very large cold finger to trap

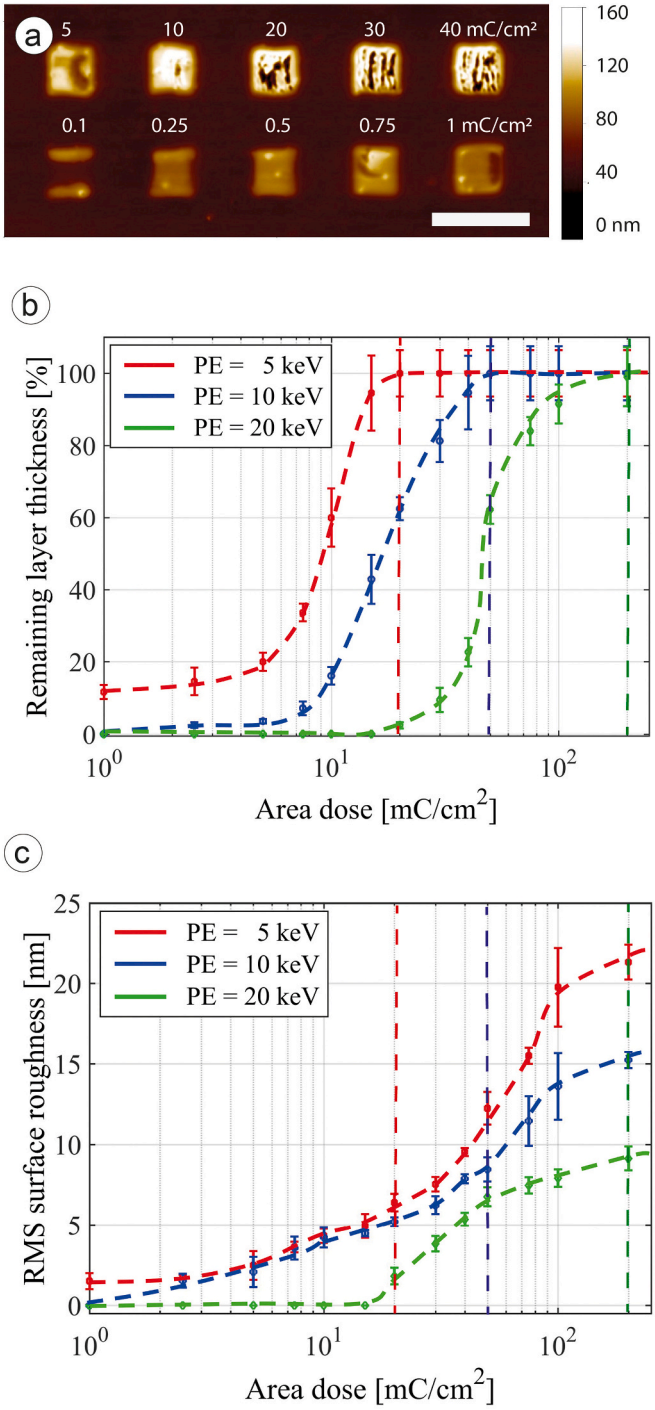

Fig. 4. Tungsten precursor ice is exposed at different electron doses and energies. (a) AFM images of 10 squares exposed at 5 keV and the area dose range 0.1 to 40 mC/cm^2. Scale bar is 10 μm. (b) Cross-linked tungsten precursor layer thickness with respect to area dose. The vertical dashed lines are critical doses for different PE energies. (c) Surface roughness vs. area dose.

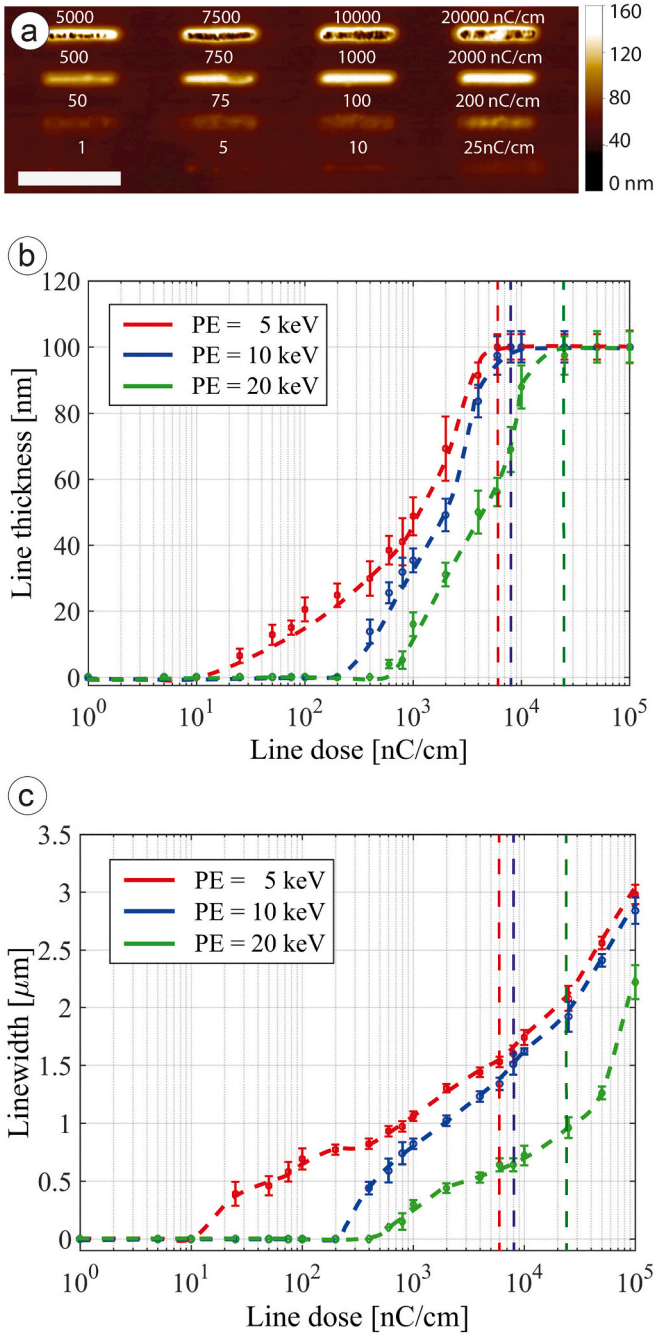

Fig. 5. IL using $W(CO)_6$. (a) AFM images of cross-linked $W(CO)_6$. The scale bar is 10 μm. (b) Remaining layer thickness and (c) line linewidth with respect to the line dose for different primary electron (PE) energies. The vertical dashed lines are critical doses for different PE energies.

water near the sample [6,17], we did not observe significant interference caused by water contamination [16]. Fig. 5b shows the cross-linked line pattern thickness increase with line-dose. For the PE energy of 5, 10 and 20 keV, the line-dose of 6, 8, and 50 μC/cm were required to cross-link a 100-nm-thick tungsten precursor ice layer fully. Fig. 5c shows the linewidth increases with dose. For the 5 keV PE, the linewidth increases from 0.4 μm to 3 μm. For 20 keV, the linewidth increases from 0.1 μm to 2.2 μm. The dose-dependent linewidth is caused by electron scattering. High-energy electrons scatter less than low-energy electrons while passing through the resist. Hence, high PE energy is preferred for high-resolution patterning, which aligns well with electron beam lithography. However, the drawback is increased surface roughness.

XPS spectra were collected to investigate the surface composition and chemical states of the IL deposited tungsten-containing structures. The full survey scan is shown in Fig. 6a, demonstrating the presence of W, C, and O elements. The signals of Au are also pronounced, which is supposed to be due to the Au electrode uncovered by IL tungsten patterns on sample surfaces. The High-resolution XPS spectrum of O 1 s is shown in Fig. 6b, which is consisted of two peaks. The peak at 532.8 eV are attributed to C—O and C═O, which agrees with the earlier studies of

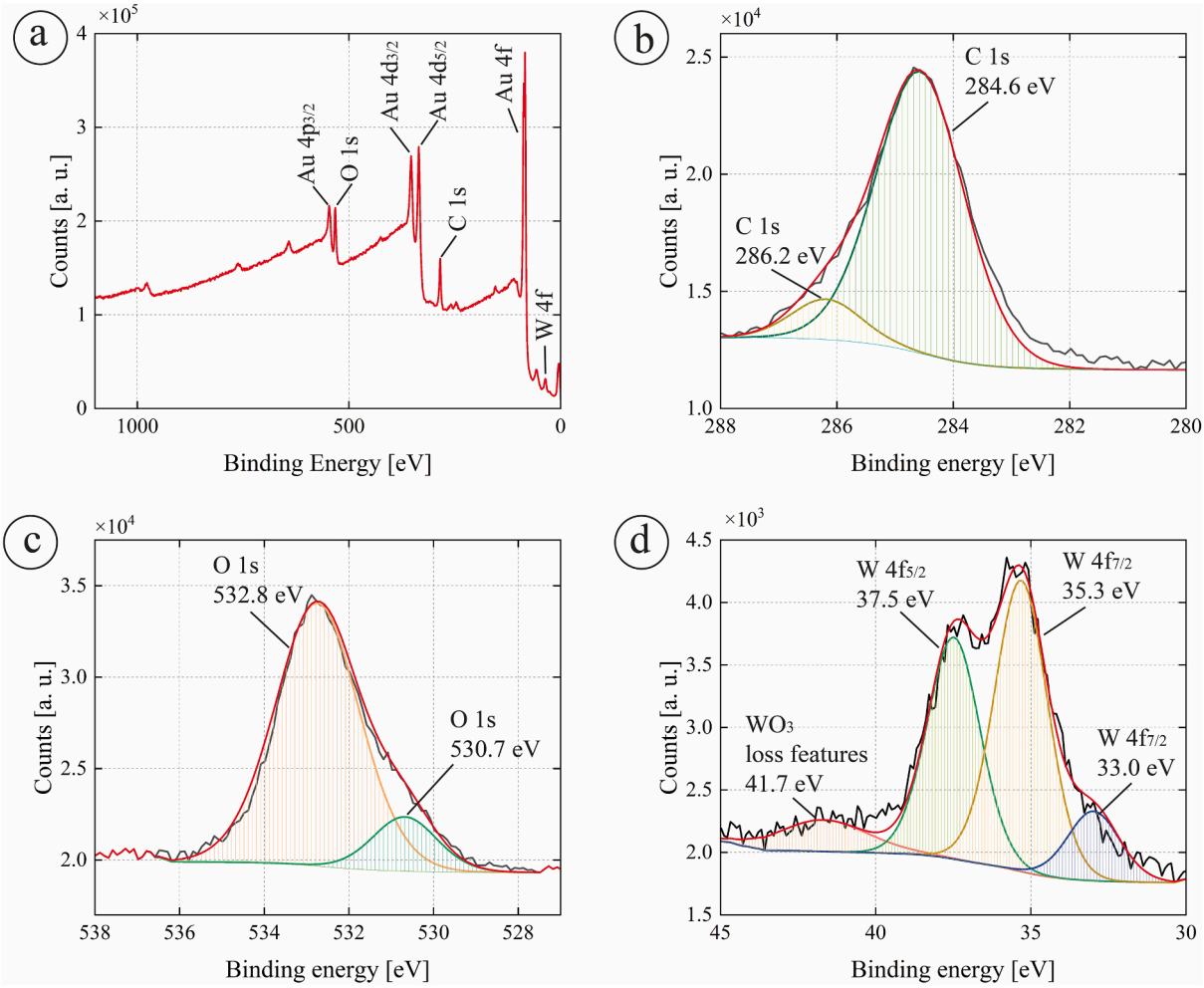

Fig. 6. XPS spectra of IL deposited tungsten ice patterns. (a) Full survey scan; (b) High resolution C 1 s spectrum; (c) High resolution O 1 s spectrum; (d) High resolution spectrum showing W 4f orbitals.

$W(CO)_6$ gas and electron interactions [23]. The O 1 s peak at 530.7 eV (Fig. 6c) is likely associated with metal oxide (in this case WO_3 or WO_2), which is in good agreement with WO_3 films deposited by chemical vapor deposition [24]. High-resolution XPS spectrum of C 1 s demonstrates two peaks at 286.2 eV and 284.6 eV. The peak centered at 284.6 eV can be attributed to graphite-like carbon, which can originate from $W(CO)_6$ or possible carbon contamination on the sample surface. The presence of the smaller peak (at 286.2 eV) has been interpreted as a conversion of CO ligands to CO molecules adsorbed on W atoms [25]. Since no peak can be observed at 283.1–283.6 eV, there is no evidence for the formation of tungsten carbide species [26], which is different compared with the results from FEBID [15,16]. The W 4f signals are weaker than C 1 s and O 1 s, and the orbitals are shown in Fig. 6d. No metallic W signals are observed. Three W peaks are presented at 37.5 eV, 35.3 eV and 33.0 eV, corresponding to W $4f_{5/2}$, W $4f_{7/2}$ and W $4f_{7/2}$. The relative intensity of the peaks at 37.5 eV and 35.3 eV suggests a more pronounced existence of WO_3 compared to WO_2 [27]. Rosenberg et al. studied the XPS spectrum of FEBID-deposited $W(CO)_6$, when the applied electron dose increases up to 4.5×10^{17} e^-/cm^2 (corresponding to a charge dose of 42 mC/cm^2). Based on the evolution of XPS spectra, the authors suggested a deposition process with CO desorption followed by the decomposition of CO ligands, resulting in oxidized W atoms embedded in a carbonaceous matrix [25]. As the XPS signals in our experiments are similar to the FEBID results, a comparable chemical component is generated during the IL process. Hence, we anticipated the cross-linked $W(CO)_6$ was an insulator, and indeed our electrical measurements of micro and nanowires confirmed the insulator properties. We were not able to reliably measure the W:C:O ratios, because the tungsten EDX spectrum was overlapping with the substrate Si EDX spectrum. To have a more thorough understanding of the cross-linking process, other techniques can be necessary, e.g., mass spectrometry [28,29] and in-situ spectroscopic ellipsometry [30].

We investigated the IL deposited $W(CO)_6$ as an etch mask for silicon. The etch rates were measured for IL deposited $W(CO)_6$ patterns on a Si substrate. A time multiplexed Bosch process was performed (see Materials and Methods for details), and the etch rate was 30 times slower than the Si etch rate. Thus, the selectivity of Si over IL deposited $W(CO)_6$ was 30:1, which is comparable with commercially available photoresists and our previous worked using nonane ice [8]. After pattern transfer into the silicon, the masking material must be removed without damaging the underlayer silicon. To remove the cross-linked tungsten hexacarbonyl, we used a fluorine-based plasma to etch it. Fluorine-based plasma etches tungsten and yields the volatile tungsten fluoride (WF_x) etching products, and we expected an efficient etching of cross-linked tungsten hexacarbonyl. The coil power and platen power were set to be 1000 W and 200 W respectively, the processing pressure was 5 mTorr and CF_4 gas flow was 20 sccm. The anticipated fast etch rate of cross-linked tungsten hexacarbonyl ice structures was measured to 500 nm/min which is 10 times faster than the etch rate of SiO_2. Buffered-hydrofluoric (HF) acid solution (12% HF with ammonium fluoride) could also etch the masking material, and the etch rate of IL tungsten hexacarbonyl was 80 nm/min, which is comparable to SiO_2 etching (90 nm/min). Cross-

linked tungsten hexacarbonyl cannot be removed by organic solvents like acetone. BHF and fluorine base plasma can be used to remove cross-linked hexacarbonyl without severely damaging the underlying silicon or silicon dioxide.

4. Conclusion

We presented IL patterning of the negative tone metalorganic tungsten hexacarbonyl on a silicon substrate held at 80 K. The IL process allows the micro- and nanoscale patterning using the electron-solid interaction principle. Study confirms that the thickness and surface roughness of the pattern increase with increasing area dose; and similarly, the line thickness and linewidth of line patterns increases with rising line doses. For the increasing PE acceleration voltage from 5 keV to 20 keV, 10 times higher area dose of 200 mC/cm^2 was needed to fully cross-link the 100 nm tungsten ice resist layer. The critical line dose increases by 233% from 6 μC/cm to 20 μC/cm when increasing PE from 5 keV to 20 keV. The linewidth decreases with the increasing PE acceleration voltage. Studies showed that IL $W(CO)_6$ patterns contained oxidized tungsten embedded in a carbon and oxygen matrix, which is very different from FEBID and cryo-FIBID studies which deposits conducted electricity attributed to WC, metallic W and Ga ions. Finally, IL pattered tungsten is tested as an etch mask, which exhibits selectivity like commercially available photoresists and nonane ice resist [8]. Compared with FEBID, because IL has larger interaction volume between electrons and the tungsten precursors, higher production throughput is achieved. IL of tungsten hexacarbonyl is 3 orders of magnitude faster than FEBID, which agree well with our previous results using organic ices without metals [8].

We envision exciting future research in three areas; (i) IL enables metal containing EBL resists that potentially enable superior resist chemistry and lithography performance. (ii) Direct patterning by cross-linking of functional materials. (iii) Layer-by-layer patterning mechanism makes IL feasible for sub-micrometer additive manufacturing or 3D printing.

Declaration of Competing Interest

The authors declare that they have no known competing financial interests or personal relationships that could have appeared to influence the work reported in this paper.

Data availability

Data will be made available on request.

Acknowledgments

The research leading to these results has received funding from the European Union's Horizon 2020 research and innovation program under the Marie Sklodowska-Curie grant agreement no. 754462 (EuroTechPostdoc) to RIH. The work presented in this article is supported by the Lundbeck Foundation, grant R305-2018-2779, and the Novo Nordisk Foundation, grant NNF0064289. AH acknowledges the support from the Marie and B. Richters Foundation.

References

[1] A. Han, D. Zhao, M. Qiu, Ice lithography, in: J.M.D. Teresa (Ed.), Nanofabrication, IOP Publishing, Bristol, UK, 2020, 9–1 to 9–27.
[2] A. Han, D. Vlassarev, J. Wang, J.A. Golovchenko, D. Branton, Ice lithography for nanodevices, Nano Lett. 10 (2010) 5056–5059, https://doi.org/10.1021/nl1032815.
[3] D. Zhao, A. Han, M. Qiu, Ice lithography for 3D nanofabrication, Sci. Bull. 64 (2019) 865–871, https://doi.org/10.1016/j.scib.2019.06.001.
[4] Shan Wu, Ding Zhao, Min Qiu 3D nanoprinting by electron-beam with an ice resist, ACS Appl. Mater. Interfaces 14 (2021) 1652–1658, https://doi.org/10.1021/acsami.1c18356.
[5] A. Han, J. Chervinsky, D. Branton, J.A. Golovchenko, An ice lithography instrument, Rev. Sci. Instrum. 82 (2011), 065110, https://doi.org/10.1063/1.3601005.
[6] W. Tiddi, A. Elsukova, M. Beleggia, A. Han, Organic ice resists for 3D Electron-beam processing: instrumentation and operation, Microelectron. Eng. 192 (2018) 38–43, https://doi.org/10.1016/j.mee.2018.01.021.
[7] A. Elsukova, A. Han, D. Zhao, M. Beleggia, Effect of molecular weight on the feature size in organic ice resists, Nano Lett. 18 (2018) 7576–7582, https://doi.org/10.1021/acs.nanolett.8b03130.
[8] W. Tiddi, A. Elsukova, H.T. Le, P. Liu, M. Beleggia, A. Han, Organic ice resists, Nano Lett. 17 (2017) 7886–7891, https://doi.org/10.1021/acs.nanolett.7b04190.
[9] H. Plank, R. Winkler, J. Sattelkow, J.D. Fowlkes, P.D. Rack, 3D Nanoprinting via focused Electron beams, Microsc. Microanal. 24 (2018) 346–347, https://doi.org/10.1017/S1431927618002222.
[10] G.M. King, G. Schürmann, D. Branton, J.A. Golovchenko, Nanometer patterning with ice, Nano Lett. 5 (2005) 1157–1160, https://doi.org/10.1021/nl050405n.
[11] P. Orús, F. Sigloch, S. Sangiao, J.M. De Teresa, Cryo-focused ion beam-induced deposition of tungsten–carbon nanostructures using a thermoelectric plate, Appl. Sci. 11 (2021) 10123, https://doi.org/10.3390/app112110123.
[12] A. Salvador-Porroche, S. Sangiao, P. Philipp, P. Cea, J.M.D. Teresa, Optimization of Pt-C deposits by Cryo-FIBID: substantial growth rate increase and quasi-metallic behaviour, Nanomaterials 2020 (1906) 10, https://doi.org/10.3390/nano10101906.
[13] M. Bresin, M. Toth, K.A. Dunn, Direct-write 3D nanolithography at cryogenic temperatures, Nanotechnology 24 (2013), 035301, https://doi.org/10.1088/0957-4484/24/3/035301.
[14] F. Porrati, R. Sachser, M. Huth, The transient electrical conductivity of W-based Electron-beam-induced deposits during growth, Irradiation and Exposure to Air, Nanotechnology 20 (2009), 195301, https://doi.org/10.1088/0957-4484/20/19/195301.
[15] T.J. Blom, T.W. Mechielsen, R. Fermin, M.B.S. Hesselberth, J. Aarts, K. Lahabi, Direct-write printing of Josephson junctions in a scanning Electron microscope, ACS Nano 15 (2021) 322–329, https://doi.org/10.1021/acsnano.0c03656.
[16] S. Barth, M. Huth, F. Jungwirth, Precursors for direct-write nanofabrication with electrons, J. Mater. Chem. C 8 (2020) 15884–15919, https://doi.org/10.1039/D0TC03689G.
[17] R.I. Haque, A.K. Waafi, K. Jaemin, D. Briand, A. Han, 80 K cryogenic stage for ice lithography, Micro Nano Eng. 14 (2022), 100101, https://doi.org/10.1016/j.mne.2021.100101.
[18] K.K. Lai, H.H. Lamb, Tungsten chemical vapor deposition using tungsten Hexacarbonyl: microstructure of as-deposited and annealed ®lms, Thin Solid Films 8 (2000).
[19] M.Z. Faizullin, A.V. Vinogradov, V.P. Koverda, Hydrate formation in layers of gas-saturated amorphous ice, Chem. Eng. Sci. 130 (2015) 135–143, https://doi.org/10.1016/j.ces.2015.03.032.
[20] A. Sevy, R.F. Huffaker, M.D. Morse, Bond dissociation energies of tungsten molecules: WC, WSi, WS, WSe, and WCl, J. Phys. Chem. A 121 (2017) 9446–9457, https://doi.org/10.1021/acs.jpca.7b09704.
[21] Y.M. Georgiev, W. Henschel, A. Fuchs, H. Kurz, Surface roughness of hydrogen Silsesquioxane as a negative tone Electron beam resist, Vacuum 77 (2005) 117–123, https://doi.org/10.1016/j.vacuum.2004.07.080.
[22] V. Constantoudis, E. Gogolides, G.P. Patsis, A. Tserepi, E.S. Valamontes, Characterization and simulation of surface and line-edge roughness in photoresists, J. Vac. Sci. Technol. B 19 (2001) 2694, https://doi.org/10.1116/1.1420582.
[23] F. Zaera, Tungsten Hexacarbonyl Thermal Decomposltlon on Nl(100) Surfaces, J. Phys. Chem 96 (1992) 4609–4615.
[24] D. Gogova, K. Gesheva, A. Kakanakova-Georgieva, M. Surtchev, Investigation of the structure of tungsten oxide films obtained by chemical vapor deposition, Eur. Phys. J. AP 11 (2000) 167–174, https://doi.org/10.1051/epjap:2000159.
[25] S.G. Rosenberg, M. Barclay, D.H. Fairbrother, Electron induced reactions of surface adsorbed tungsten Hexacarbonyl (W(CO)6), Phys. Chem. Chem. Phys. 15 (2013) 4002, https://doi.org/10.1039/c3cp43902j.
[26] J. Luthin, C. Linsmeier, Carbon films and carbide formation on tungsten, Surf. Sci. 454–456 (2000) 78–82, https://doi.org/10.1016/S0039-6028(00)00181-3.
[27] O.Yu. Khyzhun, XPS, XES and XAS studies of the electronic structure of tungsten oxides, J. Alloys Compd. 305 (2000) 1–6, https://doi.org/10.1016/S0925-8388(00)00697-6.
[28] J. Jurczyk, L. Pillatsch, L. Berger, A. Priebe, K. Madajska, C. Kapusta, I. B. Szymańska, J. Michler, I. Utke, In situ time-of-flight mass spectrometry of ionic fragments induced by focused Electron beam irradiation: investigation of Electron driven surface chemistry inside an SEM under high vacuum, Nanomaterials 12 (2022) 2710, https://doi.org/10.3390/nano12152710.
[29] M. Neustetter, F.F. da Silva, S. Denifl, Electron interactions with the focused Electron beam Inducedprocessing (FEBID) precursor tungsten Hexachloride, Rapid Commun. Mass Spectrom. 30 (2016) 1139–1144, https://doi.org/10.1002/rcm.7542.
[30] S. Vallon, B. Drévillon, F. Poncin-Epaillard, In situ spectroellipsometry study of the crosslinking of polypropylene by an argon plasma, Appl. Surf. Sci. 108 (1997) 177–185, https://doi.org/10.1016/S0169-4332(96)00574-0.